Adaptive grayscale compressive spectral imaging using optimal blue noise coding patterns

Nelson Diaz[b,*], Carlos Hinojosa[a], Henry Arguello[a]

[a]*Department of System Engineering and Informatics, Universidad Industrial de Santander, Bucaramanga 680002 Colombia*
[b]*Department of Electrical Engineering, Universidad Industrial de Santander, Bucaramanga 680002 Colombia*

Abstract

Imaging spectroscopy collects the spectral information of a scene by sensing all the spatial information across the electromagnetic wavelengths and are useful for applications in surveillance, agriculture, and medicine, etc. In contrast, compressive spectral imaging (CSI) systems capture compressed projections of the scene, which are then used to recover the whole spectral scene. A key component in such optical systems is the coded aperture which performs the scene codification and defines the sensing scheme of the system. The proper design of the coded aperture entries leads to good quality reconstructions with few compressed measurements. Commonly, the acquired measurements are prone to saturation due to the limited dynamic range of the sensor, however, the saturation is not usually taking into account in the coded aperture design. The saturation errors in compressed measurements are unbounded leading to poor reconstructions since CSI recovery algorithms only provide solutions for bounded or noisy-bounded errors. This paper proposes an adaptive grayscale coded aperture design which combines the advantages of blue noise and block-unblock coding patterns. Blue noise coding patterns are optimal and provide high-quality image reconstructions on regions of non-saturated compressed pixels. On the other hand, the block-unblock coding patterns provide redundancy

---

[*]Corresponding author
   Email address: `nelson.diaz@saber.uis.edu.co` (Nelson Diaz)

in the sampling which helps to reduce the saturation in the detector. Further, the saturation is reduced between snapshots by using an adaptive filter which updates the entries of the grayscale coded aperture based on the previously acquired measurements. The proposed coded apertures are optimized such that the number of saturated measurements is minimized. Extensive simulations and an experimental setup were made using the coded aperture snapshot spectral imager (CASSI) sensing scheme, where the results show an improvement up to 2 dB of peak signal-to-noise ratio is achieved when the proposed adaptive grayscale blue noise and block-unblock coded aperture (AGBBCA) design is compared with adaptive grayscale block-unblock coded apertures (AGBCA).

Keywords: Compressive spectral imaging, spectral imaging systems, coded aperture design, grayscale coded aperture, adaptive imaging, computational imaging

1. Introduction

Spectral imaging (SI) captures the spectral information of a scene by sensing a large amount of spatial information at different electromagnetic radiation frequencies. Spectral images are regarded as three-dimensional datasets or data cubes with two dimensions in the spatial domain (x, y) and one in the wavelength domain (λ). Knowledge of the spectral content at various spatial locations from a scene can be a valuable tool for many applications [1, 2, 3, 4, 5]. In general, traditional sensing techniques construct a spatio-spectral data cube by scanning the scene, either spectrally or spatially in proportion to the desired spatial or spectral resolution, which in turn, increases acquisition times. These techniques require to sense every single voxel of the 3D scene, hence huge storage capacities and computational resources are necessary in order to store and process such high dimensional images.

Recently, Compressive Spectral Imaging (CSI) has emerged as a new approach which acquires compressed 2D projections of the entire data cube rather than direct measurements of all voxels [6]. This enables to sense and simul-

2

taneously reduce the data dimensionality without any further processing step. Additionally, the cost of sensing, storing, transmitting and processing a spectral image acquired using this approach is reduced. In order to acquire the compressed measurements, CSI devices use an optical coding element such as a coded aperture which modulates the scene, and a dispersive element to obtain the spectral component of the image. According to their optical configuration, CSI devices employ different sampling strategies which allow exploiting statistical properties of spectral data, leading to different sensing performance in terms of spectral reconstruction quality.

The coded aperture snapshot spectral imager (CASSI) is a CSI device that comprises five optical elements[7, 8]: an objective lens which forms an image of the scene in the coded aperture plane; a coded aperture which modulate the spatial information over the complete wavelength range; a relay lens that transmits the coded light field onto a dispersive element which disperses the light before it impinges on the focal plane array (FPA). In the mathematical model of CASSI, the structure of the system sensing matrix is mainly determined by the coded aperture elements and the dispersion effect. Given a set of CASSI measurements and assuming that the spectral image can be represented as a S-sparse signal in a given basis, where S denotes the sparsity, the compressive sensing theory (CS) states that the underlying spectral scene can be reconstructed solving a convex optimization problem [9, 6, 10].

In CASSI, a spectral image $\mathbf{F} \in \mathbb{R}^{N \times N \times L}$, with L spectral bands and $N \times N$ pixels of spatial resolution, is first modulated by the coded aperture and then dispersed by the prism obtaining a set of $N \times V$ compressed measurements, with $V = N + L - 1$, yielding a compression ratio of $NV/N^2 L \approx 1/L$. In general, CSI establishes that $NV \gtrsim S \log(N^2 L) \ll N^2 L$ compressed projections are sufficient to recover $\mathbf{F}$ with high probability [6]. Although it has been shown that a single snapshot provides good reconstructions, multiple additional measurements are required for spatially detailed or spectrally rich scenes. For this reason, CSI devices enable multiple snapshot acquisition to improve the spectral image reconstructions [11, 6]. Given that each CASSI snapshot simultaneously adds

NV compressive measurements, the total number of available measurements when K snapshots are taken is KNV. In the CASSI multishot approach, a digital micromirror device (DMD) is used to change the coding pattern, before each snapshot, and remains fixed during the integration time of the detector [12]. As each snapshot acquisition is performed with a different coding pattern, different compressed measurements are captured each time. Besides acquiring multiple snapshots, different research works have shown that properly designing the coded aperture pattern is critical in order to improve the quality of image reconstruction[13, 14, 15, 16].

In the traditional CASSI system, the coded aperture is a block-unblock spatial light modulator (BCA), in which each spatial position is either a transparent or opaque element that blocks or lets all the spectral information of the pixels to pass through, so the source is uniformly encoded across wavelengths [6]. Using BCA, the compressive measurements are subject to saturation when the illumination exceeds the dynamic range of the FPA. The errors that yield saturation are unbounded and compressive sensing recovery algorithms only provide solutions for bounded errors [17]. CASSI can be implemented with the most common sensor devices such as a charge-coupled device (CCD) or a complementary metal-oxide-semiconductor (CMOS). These sensors have a limited dynamic range, for instance, a detector with 16-bits is able to measure $2^{16} = 65536$ intensity levels.

In the literature, there are different approaches to deal with saturated measurements. For instance, in [17], two approaches are proposed: the first method remove the saturation by discarding saturated measurements and then performing signal recovery using the remaining ones; the second approach deals with saturation by incorporating the saturated measurements as constraints in the recovery optimization problem. On the other hand, recent approaches propose to avoid the saturation and to increase the dynamic range of the system by improving the incoming light modulation using grayscale-adaptive coded apertures (GCA), which can be also implemented using a DMD [18]. Specifically, the GCA takes advantage of the fast switching time of the micro-mirrors which

4

enables the use of a pulse-width modulation technique for the production of grayscale values. Furthermore, the coding pattern of the next snapshot is adaptively generated, through a computer real-time model (Feedback), taking into account the current obtained compressed measurements set and a penalization function [18, 19]. However, these design approaches rely on randomly generated patterns to adaptively produce the next coded apertures.

In CASSI, it is possible to optimally design a set of coded apertures that minimizes the number of FPA snapshots while attaining the highest-quality reconstruction [20]. Therefore, in this work, we rely on such optimally designed coding patterns to produce grayscale coded apertures using an adaptive model. The proposed method efficiently improve the quality of image reconstruction by reducing the saturation of compressed measurements while the dynamic range of the sensor is increased. This paper is organized as follows: first, the mathematical model of the sensing process behind CASSI multishot system is described. Then, the optimal blue noise coding patterns design and the FPA saturation in CASSI are presented. Subsequently, the proposed adaptively designed grayscale coded aperture (AGBBCA) is developed. Finally, simulations are performed to test the quality of the proposed coded aperture design.

2. CASSI System

2.1. CASSI Continuous and Discrete Model

The CASSI sensing process is depicted in Fig. 1. In the ℓ-th CASSI snapshot, the spatio-spectral density source $f_0(x, y, \lambda)$, where (x, y) are the spatial coordinates and λ is the wavelength, is first coded by a coded aperture $T^\ell(x, y)$ and then, the resulting coded field $f_1^\ell(x, y, \lambda)$ is spectrally dispersed by a dispersive element before it impinges on the FPA as $f_2^\ell(x, y, \lambda)$,

$$f_2^\ell(x, y, \lambda) = \int \int T^\ell(x', y') f_0(x', y', \lambda) \times h(x' - \alpha D(\lambda) - x, y' - y) dx' dy', \ (1)$$

where $h(\cdot)$ is the optical impulse response of the system and $D(\lambda)$ is the dispersion function of the dispersive element which operates along the x axis. The
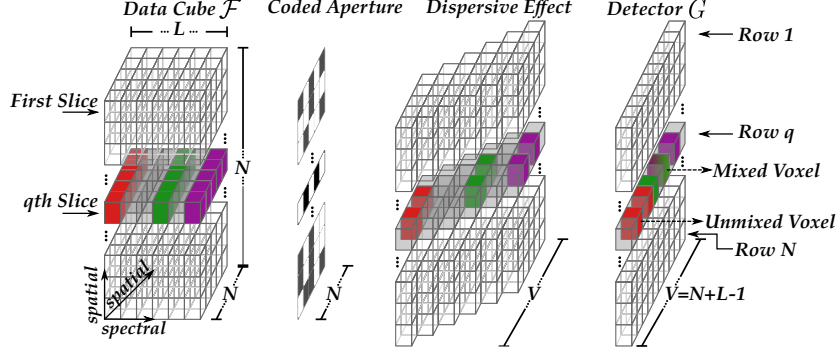
5

Figure 1: Schematic representation of the CASSI sensing process.

resulting intensity image at the FPA is the integration of the field $f_2^\ell(x, y, \lambda)$ over the detector's spectral range sensitivity.

The input spatio-spectral scene can be represented as a discrete data cube $\mathcal{F} \in \mathbb{R}^{N \times N \times L}$, with L spectral bands of $N \times N$ pixels. Each source voxel is indexed as $\mathcal{F}_{m,n,k}$, where $m = 0, \cdots, N-1$, $n = 0, \cdots, N-1$ are the discrete indices for the spatial dimensions and $k = 0, \cdots, L-1$ indexes the spectral bands. In addition, the ℓ-th coded aperture can be represented in discrete form as $\mathbf{T}^\ell \in \mathbb{R}^{N \times N}$, which entries $T_{m,n}^\ell$ have binary values that block (0) or allow the passage of light (1). Following the mathematical model in [7], the CASSI measurements can be succinctly expressed as

$$\tilde{G}_{m,n}^\ell = \sum_{k=0}^{L-1} \mathcal{F}_{m,(n-k),k} T_{m,(n-k)}^\ell + \omega_{m,n}^\ell, \qquad (2)$$

where $\tilde{G}_{m,n}^\ell$ is the intensity at the (m, n)-th position of the detector, with dimensions $N \times N + L - 1$, acquired in the ℓ-th snapshot.

In this work, we replace the block-unblock coded aperture (BCA) with a grayscale coded aperture (GCA), which also modulates the source along spectral coordinate. The modified GCA-CASSI system is depicted in Fig. 2. The spectral image codification, in the ℓ-th snapshot, is now performed by the GCA represented by $\bar{T}^\ell(x, y)$ which is applied to the spatio-spectral density source $f_0(x, y, \lambda)$, obtaining the coded field $\bar{f}_1^\ell(x, y, \lambda)$. Note that this field is differ-
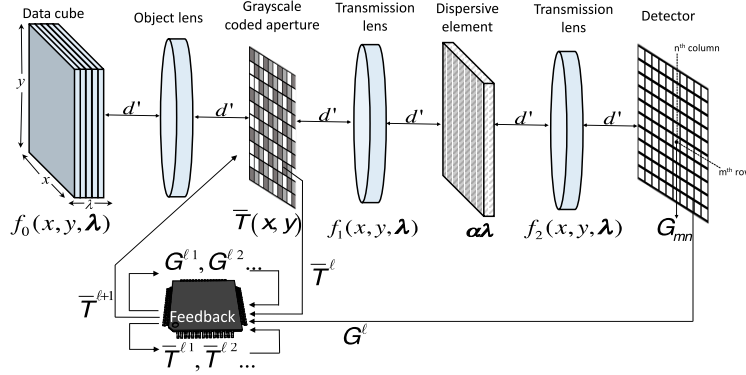
Figure 2: Sketch of the adaptive grayscale coded aperture (AGCA) CASSI system. The AGCA is composed of two modifications to the traditional CASSI. First, the BCA is replaced with the GCA in order to improve the modulation of the incoming light. On the other hand, an adaptive system allows feedback between the focal plane array and the digital micromirror device. The adaptive system uses the compressive measurements to compute the next coded aperture.

ent from $f_1^\ell(x, y, \lambda)$, which is achieved with a traditional BCA. In particular, instead of block-unblock the complete spectrum at a given spatial location, the GCA modulates the incident light in that particular spatial position taking into account the grayscale level of the GCA pixel. The discrete entries of the ℓ-th GCA $\bar{T}_{m,n}^\ell$ vary in the range $\{0 - (l-1)\}$, being l the number of grayscale levels of the DMD. In this way, Eq. (2) can be rewritten as

$$G_{m,n}^\ell = \sum_{k=0}^{L-1} \mathcal{F}_{m,(n-k),k} \bar{T}_{m,(n-k)}^\ell + \omega_{m,n}^\ell, \qquad (3)$$

where $G_{m,n}^\ell$ is the compressed value at the (m, n) position, in the ℓ-th FPA measurement acquired with a GCA coded aperture.

2.2. Matrix Model

The set of compressive measurements $\mathbf{G}^\ell$, from Eq. (3), can be expressed in vector notation as $\mathbf{g}^\ell$, so each capture of the GCA-CASSI system can be

7

modeled by

$$\mathbf{g}^{\ell} = \mathbf{H}^{\ell}\mathbf{f}, \tag{4}$$

where $\mathbf{f} = \mathrm{vec}([\mathbf{f}_0, \cdots, \mathbf{f}_{L-1}])$ is the vector representation of the spatio-spectral input source $\mathbf{F}$, being $\mathbf{f}_k$ the vectorization of the k-th spectral band, and $\mathbf{H}^{\ell}$ is a compressive projection matrix corresponding to the ℓ-th GCA coded aperture. More specifically, $\mathbf{H}^{\ell}$ is a $NV \times N^2L$ sparse matrix whose nonzero entries are determined by the grayscale values of the GCA $\bar{T}^{\ell}$, and its structure accounts for the effect of dispersion given by the prism. Taking this into account, the structure of the output $\mathbf{g}^{\ell}$ in Eq. (4) can be succinctly expressed as

$$\mathbf{g}^{\ell} = \underbrace{\begin{bmatrix} \mathrm{diag}(\bar{\mathbf{t}}) & \mathbf{0}_{N \times N^2} & \cdots & \mathbf{0}_{N(L-1) \times N^2} \\ & \mathrm{diag}(\bar{\mathbf{t}}) & \cdots & \\ & & \ddots & \\ \mathbf{0}_{N(L-1) \times N^2} & \mathbf{0}_{N(L-2) \times N^2} & \cdots & \mathrm{diag}(\bar{\mathbf{t}}) \end{bmatrix}}_{\mathbf{H}} \begin{bmatrix} \mathbf{f}_0 \\ \mathbf{f}_1 \\ \vdots \\ \mathbf{f}_{L-1} \end{bmatrix} + \omega, \tag{5}$$

where $\mathrm{diag}(\bar{\mathbf{t}})$ is an $N^2 \times N^2$ diagonal matrix whose entries are elements of the grayscale coded aperture in vector form $\bar{\mathbf{t}}$. The measurement vectors $\mathbf{g}^{\ell}$ acquired at each GCA-CASSI snapshot can be succinctly expressed in vector form as $\mathbf{g} = \left[\left(\mathbf{g}^0\right)^T, \left(\mathbf{g}^1\right)^T, \cdots, \left(\mathbf{g}^{K-1}\right)^T \right]^T$, with $\ell = 0, 1, \cdots, K-1$ snapshots. Therefore, Eq. (4) can be rewritten in the standard form of an underdetermined system of linear equations

$$\mathbf{g} = \mathbf{H}\mathbf{f}, \tag{6}$$

were $\mathbf{H} = \left[\left(\mathbf{H}^0\right)^T, \left(\mathbf{H}^1\right)^T, \cdots, \left(\mathbf{H}^{K-1}\right)^T \right]^T$ is the concatenation of all matrices $\mathbf{H}^{\ell}$.

2.3. Spectral Image Reconstruction

After the compressive measurements acquisition, the subsequent procedure is to recover the underlying 3D scene. However, the amount of acquired measurements $KN(N + L - 1)$, where $K \ll L$ is the number of measurement shots,

8

is far less than the number of 3D data cube entries to be estimated N^2L. Therefore, the spectral image reconstruction problem is ill-posed, hence it cannot be solved by directly inverting the system in Eq. (6).

The theory of compressive sensing (CS) provides an alternative method to recover the underlying spectral scene $\mathbf{f}$ from the measurement $\mathbf{g}$. In general, CS assumes that $\mathbf{f} \in \mathbb{R}^{N^2L}$ has a S-sparse representation in a given basis $\boldsymbol{\Psi}$, and there exists high incoherence between the sensing matrix $\mathbf{H}$ and $\boldsymbol{\Psi}$. Then, the measurement set $\mathbf{g}$ in Eq. (6) can be expressed as $\mathbf{g} = \mathbf{H}\boldsymbol{\Psi}\boldsymbol{\theta}$, where $\mathbf{f} = \boldsymbol{\Psi}\boldsymbol{\theta}$ and $\boldsymbol{\theta}$ is a sparse vector with $S \ll N^2L$ nonzero entries, such that $\mathbf{f}$ can be approximated as a linear combination of only S columns of $\boldsymbol{\Psi}$. Then, the inverse CS problem consist on recovering $\boldsymbol{\theta}$ such that the $\ell_2 - \ell_1$ cost function is minimized, i.e. it looks for a sparse approximation of the spatio-spectral data cube. Mathematically, the optimization problem can be written as

$$\tilde{\mathbf{f}} = \boldsymbol{\Psi}\left\{\underset{\tilde{\boldsymbol{\theta}}}{\operatorname{argmin}} \|\mathbf{g} - \mathbf{A}\tilde{\boldsymbol{\theta}}\|_2^2 + \tau\|\tilde{\boldsymbol{\theta}}\|_1\right\}, \tag{7}$$

where $\mathbf{A} = \mathbf{H}\boldsymbol{\Psi}$, $\tilde{\mathbf{f}}$ is an estimation of the underlying spectral scene and τ is a regularization parameter. The basis representation $\boldsymbol{\Psi}$ is set as the Kronecker product of three basis $\boldsymbol{\Psi} = \boldsymbol{\Psi}_1 \otimes \boldsymbol{\Psi}_2 \otimes \boldsymbol{\Psi}_3$, where the combination $\boldsymbol{\Psi}_1 \otimes \boldsymbol{\Psi}_2$ is the 2D-Wavelet Symmlet 8 basis and $\boldsymbol{\Psi}_3$ is the Discrete Cosine basis. The 2D-wavelet is used for the image compression in the spatial domain, while the Discrete Cosine basis perform compression on the spectral information.

2.4. Optimal Designed Coded Apertures

Note that the structure of $\mathbf{A}$, known as the CASSI sensing matrix, is critical in the inverse problem shown in Eq. (7) as it ultimately determines the attainable quality of reconstruction. As the basis $\boldsymbol{\Psi}$ is fixed, the structure of $\mathbf{A}$ is determined by the same optical elements as in the projection matrix $\mathbf{H}$, i.e., the structure of $\mathbf{A}$ is determined by the dispersive effect, given by the prism, and the non-zero coefficients are defined by the coded aperture used in each measurement shot, which is the only non-fixed element.

9

Accordingly, different research works have focused on optimally design the set of coded apertures in order to forge a structure on $\mathbf{A}$ that minimizes the required number of FPA snapshots while attaining the highest-quality reconstruction. Commonly, such works take into account the restricted isometry property (RIP) of the sensing matrix and the correlation between $\mathbf{H}$ and $\mathbf{\Psi}$ as the coded apertures design criteria [15, 20, 13, 19]. Particularly, in order to guarantee a correct recovery of the underlying signal, CS requires the acquired measurements to be uncorrelated, and the coherence is used to measure the correlation between $\mathbf{H}$ and $\mathbf{\Psi}$, such that the CS condition hold. The coherence of CASSI sensing matrix can be calculated as

$$\mu = \max_{i \neq j} |\mathrm{TPSF}(i,j)| / \sqrt{\mathrm{TPSF}(i,i)\mathrm{TPSF}(j,j)}, \tag{8}$$

where $\mathrm{TPSF}(i,j) = (\mathbf{\Psi}^T \mathbf{H}^T \mathbf{H} \mathbf{\Psi})_{i,j}$ is a transform point-spread function, as defined in [21, 22]. Then, as we are interested in how uncorrelated are the matrices $\mathbf{H}$ and $\mathbf{\Psi}$, the incoherence can be defined as $\tilde{\mu} = 1 - \mu$.

On the other hand, the RIP establishes necessary conditions for $\mathbf{A}$ such that the ℓ_2 norm of the underlying 3D spectral image is approximately preserved under the transformation $\mathbf{A}\boldsymbol{\theta}$. Specifically, if the matrix $\mathbf{A}$ satisfies the RIP, then there exists a restricted isometry constant δ such that $(1 - \delta)\|\boldsymbol{\theta}\|_2 \leq \|\mathbf{A}\boldsymbol{\theta}\|_2 \leq \|\boldsymbol{\theta}\|_2(1 + \delta)$ [23, 15]. The RIP requires that all $\tilde{m} \times |\mathcal{T}|$ column submatrices $\mathbf{A}_{|\mathcal{T}|}$ of $\mathbf{A}$ are well conditioned for all $|\mathcal{T}| \leq S$, where $\tilde{m} = KN(N + L - 1)$. This is equivalent that all eigenvalues of matrices $\mathbf{A}_{|\mathcal{T}|}^T \mathbf{A}_{|\mathcal{T}|}$ are in the interval $[1 - \delta, 1 + \delta]$. The probability that this condition is satisfied can be calculated by estimating the statistical distribution of the maximum eigenvalue λ_{max} of the matrices $\mathbf{A}_{|\mathcal{T}|}^T \mathbf{A}_{|\mathcal{T}|} - \mathbf{I}$, where $\mathbf{I}$ is an identity matrix. The λ_{max} distribution is estimated using concentration of measure for random matrices developed in [24].

Recently a coded aperture design whose nonzero coefficient distribution exhibits spatiotemporal characteristics of blue noise patterns, that suppress low-frequency components of noise, has been developed. Specifically, Authors in

10

[20] present an optimally-designed coded aperture set such that the RIP of $\mathbf{A}$ is satisfied with high probability and $\mathbf{H}$ presents high incoherence with respect to the sparse representation basis $\mathbf{\Psi}$. In general, the spatiotemporal blue noise

coded aperture (BN) design relies on three criteria: horizontal separation, vertical separation, and temporal correlation. The algorithm that generates the BN coded apertures, first opens a local window U_p^ℓ, of size $\Delta \times \Delta$, centered at the same point in each coded aperture $\mathbf{T}^\ell$, for $\ell = 0, 1 \cdots, K-1$, and then sums the number of ones in the vertical, horizontal and diagonal directions. Using

these quantities, a metric is calculated taking into account four given weights. Finally, for each spatial location, the algorithm inserts the nonzero element in the coded aperture with the minimum concentration of ones in the window. Figure 3. shows a comparison between a block-unblock coded aperture, and a BN coded aperture. In addition, the corresponding quality of image reconstruction,

in terms of peak signal-to-noise ratio (PSNR), is depicted for the block-unblock 36.7955 dB, and BN 40.5729 dB, using 8 snapshots in both cases. It can be noted that the concentration (clusters) of ones in the resulting coded aperture is considerably minimized which entails high incoherence with respect to the sparse representation basis and that the RIP is satisfied with high probability.

2.5. FPA saturation in CASSI

The FPA Saturation appears when the number of measurements exceeds the dynamic range of the sensor quantizer [18]. The finiteness of dynamic range is due to two reasons: the first is related to physical limitations that allow a finite range voltage to be correctly converted to bits; the second is that only a

finite number of bits are available to represent each value. Quantization with saturation is referred to as finite-range quantization [25]. The noise imposed by such finite-range quantization is unbounded. However, CS recovery techniques only provide guarantees for bounded noise or bounded with high probability [25]. Therefore, dealing with saturation in CASSI is an important issue since

it reduces the attainable reconstruction quality. Figure 4 shows examples of compressive measurements, generated using Equation 3, four distinct percent-
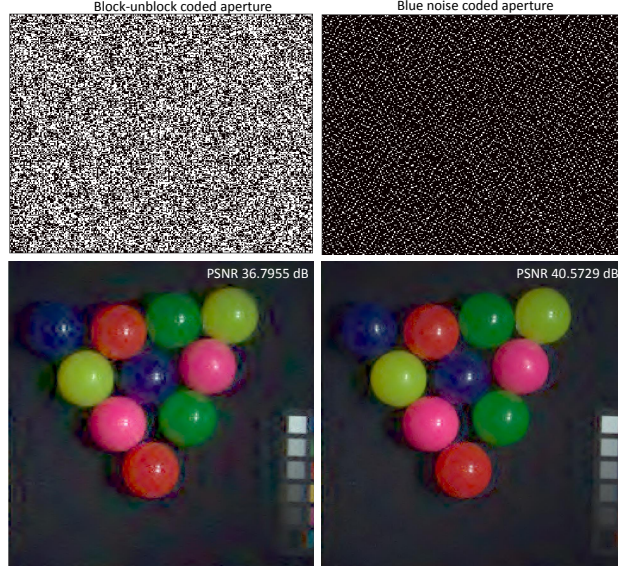
Figure 3: Example of a block-unblock coded aperture and BN coded aperture and their corresponding image reconstruction. The quality of image reconstruction for block-unblock 36.7955 dB, and blue noise 40.5729 dB.

ages of saturated pixels (0%, 10% and 20%, and 30% respectively), and their corresponding attained reconstructions using 8 shots. Notice that the higher the saturation percentage, the lower the quality of the reconstructed image. A detailed illustration of CASSI measurements saturation can be found in [18]. The FPA saturation in CASSI can be avoided by replacing the traditional BCA with a GCA coded aperture.

3. Adaptively designed grayscale coded apertures

In this section, an adaptive grayscale coded aperture design, which combines the advantages of blue noise and block-unblock coding patterns, is developed. In general, the proposed algorithm generates a blue noise coded aperture ensemble and then the saturation is reduced between snapshots by using an adaptive filter which updates the entries of the grayscale coded aperture based on the previously acquired measurements.
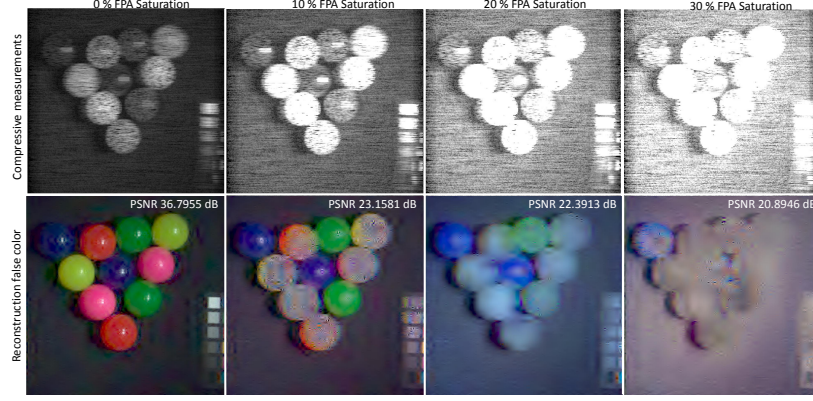
Figure 4: Compressive measurements for 4 levels of saturation and their respective image reconstruction. First row, compressive measurements with 0%, 10%, 20%, and 30% FPA saturation. Second row, the corresponding image reconstruction for 0%, 10%, 20%, and 30% using 8 snapshots. The type coded aperture is block-unblock.

3.1. Adaptive Grayscale block-unblock coded aperture

The adaptive grayscale block-unblock coded aperture (AGBCA) uses random coding patterns that follow a Bernoulli distribution. The coded aperture ensemble can be represented for all snapshots as 3D structure denoted by $\mathbf{T}_l^\ell \in \mathbb{R}^{N \times N \times L}$, where ℓ indexes a specific snapshot, and l represents the wavelength index. Given the vectorization of the 3D structure denoted by $\mathbf{t}_l^\ell = vec(\mathbf{T}_l^\ell)$. In addition, the percent of the light that reaches the sensor, known as transmittance, is 50% in the AGBCA, hence the coded aperture can be generated as $\mathbf{T}_l^\ell \sim Ber(0.5)$. Examples of the AGBCA coded aperture and the acquired compressed measurements are shown in Fig. 5. The first column represents the generated coded aperture, and the second one denotes the acquired compressed measurements for the 1,3,5 and 7 snapshot, respectively. The red region denotes the grayscale coded aperture with block-unblock spatial distribution. Notice that, in the first snapshot, the percentage of saturation in the compressive measurements is 10.52%, but the percentage of saturation is reduced at each snapshot.

13

3.2. Adaptive Grayscale blue noise and block-unblock coded aperture

The adaptive grayscale blue noise and block-unblock coded aperture (AG-BBCA) approach use a combination of blue noise and block-unblock coding patterns. Specifically, in the region of the sensor where pixels are not satu-
rated, the proposed design uses optimal blue noise coding patterns. Similarly, in regions of the sensor where pixels are saturated, the proposed design uses block-unblock coding patterns. The intuition behind this design is that blue noise coded apertures optimize the sampling since each pixel of the scene is sampled once and the distance between samples is the maximum [20], which
will satisfy the RIP with high probability. However, in a saturated scenario, many compressed measurements reach the limit of the detector's dynamic range. Due to the lack of redundancy in the sampling when optimal blue noise coded apertures are used, a re-sample of the saturated measurement is not possible. However, exploiting the redundancy of block-unblock coded apertures it is pos-
sible to re-sample in the saturated scenario. Similarly, to block-unblock coded apertures, the blue noise coded apertures can be represented as a 3D structure. Formally, $\mathbf{T}_l^\ell \sim \mathrm{BN}(1/\mathrm{L})$ represents a blue noise coded aperture in the l wavelength, described in subsection 2.4. The vectorization of all coded apertures is denoted by $\mathbf{t}_l^\ell = vec(\mathbf{T}_l^\ell)$. Examples of the proposed coded aperture AGBBCA
and compressed measurements are shown in the third and fourth column of Fig. 5, respectively. The red regions, shown in the third row, denotes the grayscale coded aperture with block-unblock spatial distribution. Notice that in the first snapshot the percentage of saturation in the compressive measurements is 10%, but the percentage of saturation is reduced at each snapshot.

3.3. Adaptive algorithm to reduce saturation using grayscale coded apertures

The algorithm receives as input the first compressive measurements and a set of K coded apertures which can be either block-unblock (AGBCA) or blue noise (AGBBCA). The output is the reconstructed datacube. The algorithm 1 iterates until the number of snapshots is reached. At the begin of line 3, using the previous compressive measurement, the algorithm creates a vector
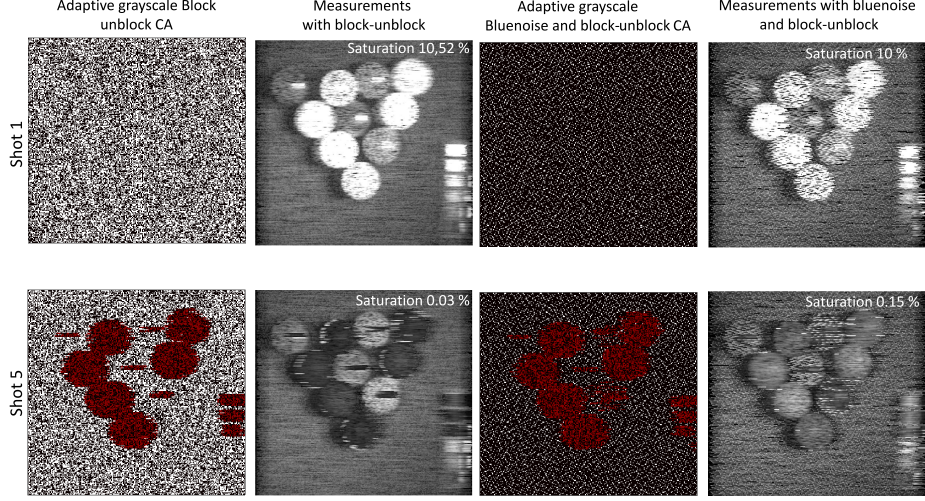
14

Figure 5: Comparison between the AGBBCA and AGBCA for 1,3,5, and 7 snapshots. The AGBBCA and the AGBCA, the red region in the coded aperture denote the portion of the coding pattern with grayscale and the corresponding compressive measurements are shown with the percentage of saturation at each snapshot.

$\mathbf{s}^\ell \leftarrow sat(\mathbf{g}^{\ell-1})$ with the number of times that a pixel in the coded aperture induces saturation in the detector. The thresholding on line 4 identifies two regions in the coded aperture, the entries involved in saturation $\mathbf{q}^\ell$, and the entries not involved in saturation $\mathbf{1} - \mathbf{q}^\ell$. Two vectors are required to compute the next coded aperture: a block-unblock coded aperture and the vectorization of the ℓth coded aperture, either block-unblock or blue noise. The next coded aperture realization is computed reducing the transmittance of the entries in the coded aperture involved with saturation, according to the previous snapshot. In more detail, the line 7 reduce the transmittance in the unblock entries to 5% of the previous value, in the region of the coded aperture which involves the saturation $\mathbf{q}^\ell$, and remains the transmittance of the unblock entries in the no saturated regions $\mathbf{1} - \mathbf{q}^\ell$.

The remaining steps of the algorithm 1 rearrange the vectorization form of $\mathbf{r}^\ell$ to the corresponding matrix $\mathbf{H}^\ell$. More precisely, in line 10, the vector $\mathbf{r}^\ell$ is rearranged as the 2D k-th plane according to $(\mathbf{r}_k^\ell)_l \leftarrow \mathbf{r}_n^\ell$. Subsequently,

15

Algorithm 1 Adaptive grayscale blue noise block-unblock coded aperture (AGBBCA).

Require: $\mathbf{g} \leftarrow [\mathbf{g}^0]^T$, $\mathbf{T} \leftarrow [(\mathbf{T}^0)^T, \ldots, (\mathbf{T}^{K-1})^T]^T$, $a = 0.05$
Ensure: $\hat{\mathbf{f}}$

1: **function** AGBBCA($\mathbf{g}$, $\mathbf{T}$)
2:     **for** $\ell \leftarrow 1, K - 1$ **do**
3:         $\mathbf{s}^\ell \leftarrow sat(\mathbf{g}^{\ell-1})$ ▷ Coded aperture pixels involved in saturation
4:         $\mathbf{q}^\ell \leftarrow (\mathbf{s}^\ell > \mathbf{0})$ ▷ Thresholding
5:         $\mathbf{t}^\ell \leftarrow vec(\mathbf{T}^\ell)$ ▷ Vectorization of coded aperture matrix
6:         $\mathbf{b}^\ell \leftarrow Ber(0.5)$ ▷ Generate block-unblock coded aperture
7:         $\mathbf{r}^\ell \leftarrow \mathbf{q}^\ell \odot \mathbf{b}^\ell + (\mathbf{1} - \mathbf{q}^\ell) \odot a\mathbf{t}^\ell$,   ▷ Next coded aperture
8:         **for** $n \leftarrow 0, N^2 L - 1$ **do**
9:             $k = \lfloor n/N^2 \rfloor$, $l = n \mod N^2$
10:            $(r_k^\ell)_l \leftarrow r_n^\ell$ ▷ Rearrange $\mathbf{r}$
11:            **for** $m \leftarrow 0, KV - 1$ **do**
12:                **if** $m - \ell_m V = n - k_n(N^2 - N)$ **then**
13:                   $(H_m^\ell)_n \leftarrow (r_{k_n}^{\ell_m})_{m - \ell_m v - k_n N}$ ▷ Compute $\mathbf{H}$
14:                **else**
15:                   $(H_m^\ell)_n \leftarrow 0$
16:         $\mathbf{g}^\ell \leftarrow \mathbf{H}^\ell \mathbf{f}$ ▷ Next snapshot
17:     $\mathbf{g} \leftarrow [(\mathbf{g}^0)^T, \ldots (\mathbf{g}^{K-1})^T]^T$
18:     $\mathbf{H} \leftarrow [(\mathbf{H}^0)^T, \ldots (\mathbf{H}^{K-1})^T]^T$
19:     **return** $\hat{\mathbf{f}} \leftarrow \mathbf{\Psi}^{-1}(\text{argmin}_{\boldsymbol{\theta}} \|\mathbf{g} - \mathbf{H}\mathbf{\Psi}\boldsymbol{\theta}\|_2^2 + \tau\|\boldsymbol{\theta}\|_1)$

---

in line 13, the vectorization of the colored coded aperture $\mathbf{r}^\ell$ is stacked in the sensing matrix $\mathbf{H}^\ell$ according to $(H_m^\ell)_n \leftarrow (r_{k_n}^{\ell_m})_{m - \ell_m v - k_n N}$, $k_n = \lfloor n/N^2 \rfloor$, $\ell_m = \lfloor m/V \rfloor$, $\ell_m \in \{0, \ldots, K-1\}$. In line 16, the adaptive snapshot is captured as $\mathbf{g}^\ell \leftarrow \mathbf{H}^\ell \mathbf{f}$. Finally, in line 19, an approximation of the datacube $\hat{\mathbf{f}}$ is obtained as the output of algorithm 1.

4. Simulations

In this section, the adaptive grayscale blue noise and block-unblock coded apertures (AGBBCA) are compared against adaptive grayscale block-unblock coded aperture (AGBCA). A set of compressive measurements is simulated using equation 6. The datasets used in the experiments are the Superballs and Glass-Tiles scenes which are shown in Fig. 6(a) and (b), respectively. The dataset was captured using a CCD camera exhibiting 256×256 of spatial resolution and 16 spectral bands. The width wavelength spans between 400 and 700 nm. The regularization parameter is set to $\tau = 0.0001$. The simulations

were realized with saturation levels between 10% and 30%. 10 dB of SNR noise was added to the AGBBCA and AGBCA compressive measurements. The basis representation is set to be $\mathbf{\Psi} = \mathbf{\Psi_1} \otimes \mathbf{\Psi_2}$ where $\mathbf{\Psi_1}$ playing the role of spatial sparsifier as the 2D-Wavelet Symmlet 8 basis, and $\mathbf{\Psi_2}$ the spectral sparsifier is the 1D-DCT basis. The MATLAB code of the simulations can be downloaded from the project repository [1].
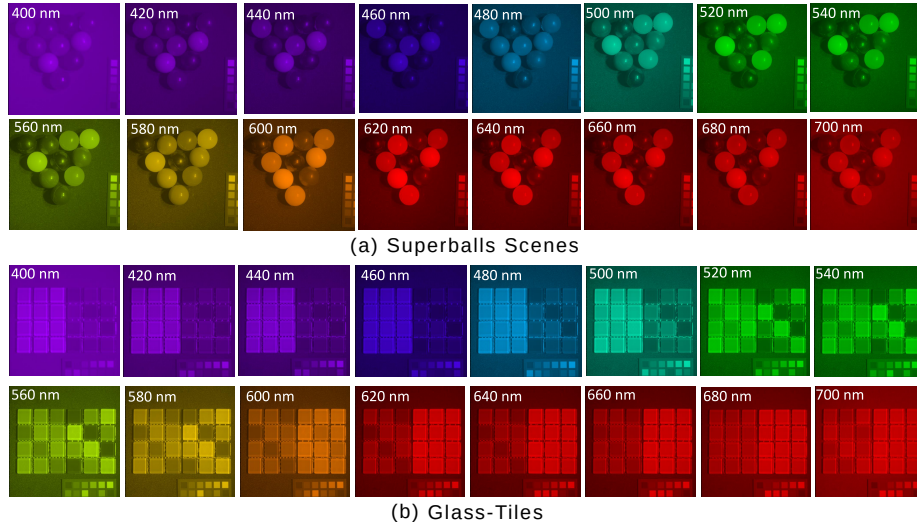

(a) Superballs Scenes

(b) Glass-Tiles

Figure 6: Datacubes used for simulations with 256×256 pixels of spatial resolution and 16 spectral bands within the range 400-700 nm. The first and second rows show the Superballs scene. The third and fourth rows correspond to the Glass-Tiles scene.

One outstanding metric to compare coded apertures is the radially averaged power spectrum density (RASPD) [26]. In the Fourier domain, the power spectrum of a coded aperture can be computed by spectral estimation. Bartlett's method is used for spectral estimation. The method is based on averaging periodograms, where a periodogram is the magnitude squared of the Fourier transform of a sample output divided by the sample size. The RASPD metric is used to determine attributes in lithography codes. In particular, the radial

---

[1] https://git.io/fjqlU

17

spectrum described by the block-unblock coded aperture is flat, in contrast, that from the blue noise coded aperture changes along the radial axis as depicted in Fig. 7 (a). The patterns used to attenuate the saturation are a hybrid between blue noise and grayscale (AGBBCA) or block unblock and grayscale (AGBCA). When the coded aperture is hybrid (AGBBCA) the radial spectrum curve is flatter in comparison with the blue noise radial spectrum as shows the Fig. 7 (b) because it is the combination of two coding patterns block-unblock and blue noise, however, it preserves some values in the high frequencies.
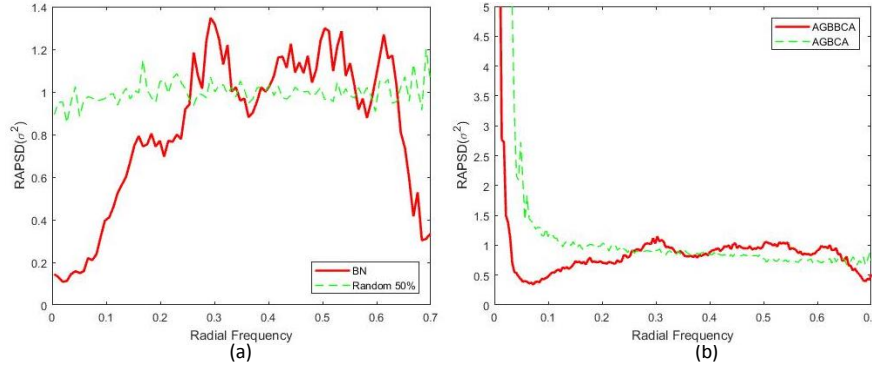
Figure 7: (a) Comparison of the radially averaged power spectral (RASPD) density for the random and BN coded apertures. (b) Comparison of RASPD for AGBBCA, and AGBCA.

Figure 8 shows the quality of reconstructions against the number of snapshots for 10%, and 20% percentage of saturation and the noise with $SNR = 10$ dB. The first row shows the quality of image reconstruction for the Superballs scene. The second row depicts the quality of image reconstruction when the scene is Glass-Tiles. The number of snapshots varies from 1 to 8. The quality of image reconstruction improves in up to 2 dB when the number of snapshots is increased, particularly, when at least 5 snapshots are captured.

Figure 9 shows the quality of reconstruction as a function of the percentage of saturation. The first, second and third rows depict the quality of image reconstruction against the percentage of saturation for 4, 6 and 8 snapshots. The noise added to the compressive measurements is $SNR = 10$ dB, and the percentage of saturation varies from 10% to 30%. In general, the quality of
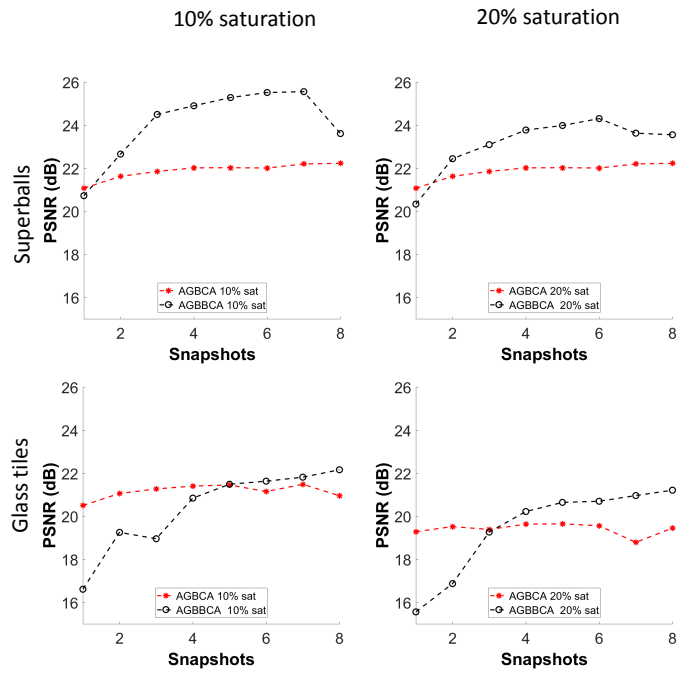
18

Figure 8: Quality of reconstruction against the number of snapshots for (first row) Superballs and (second row) Glass-Tiles scenes.
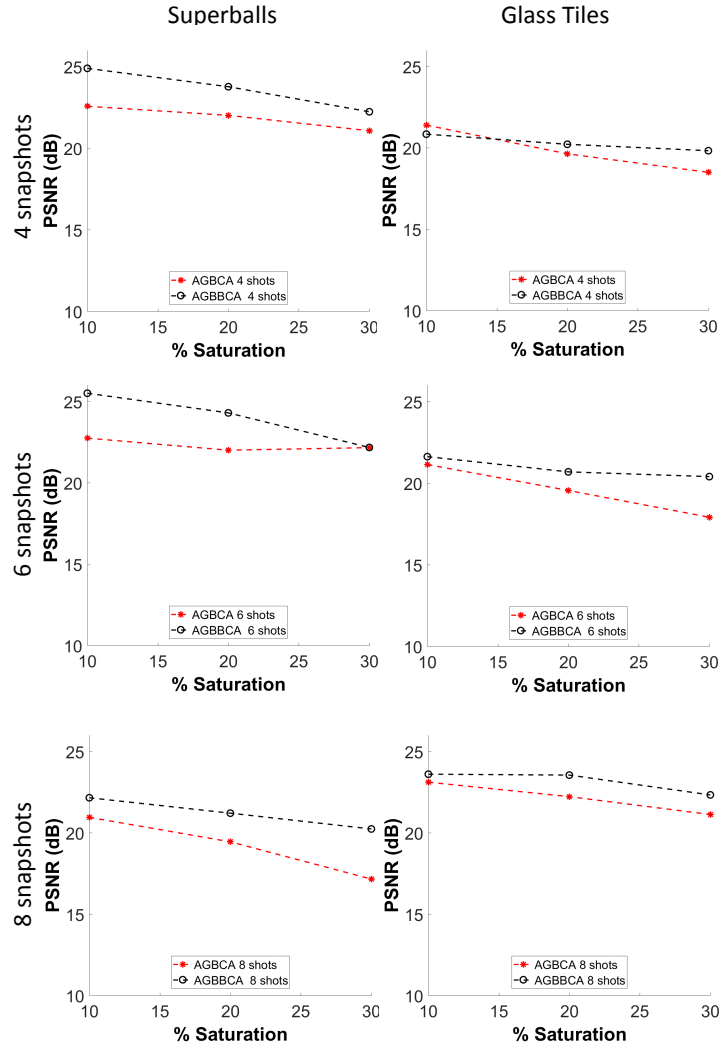
Figure 9: Quality of reconstruction against the percentage of saturation.

image reconstruction is improved in up to 2 dB when the number of snapshot increase.

Figure 10 shows RGB reconstruction with the Superballs and Glass-Tiles scene using the AGBBCA, and AGBCA, with 8 snapshots, noise with $SNR = 10$ dB, and percentage of saturation 10%. In the first row is depicted the RGB representation of Superballs scene and the corresponding reconstruction using AGBCA and AGBBCA. The quality of image reconstruction via AGBCA is PSNR=22.27 dB, in contrast, the quality of image reconstruction using AG-BBCA is PSNR=24.88 dB. The second row shows the RGB representation of Glass-Tiles scene, and the corresponding reconstruction using AGBCA and AG-BBCA. The quality of image reconstruction using AGBCA is PSNR=20.9508 dB, which is overcome by AGBBCA with PSNR=22.1557 dB.
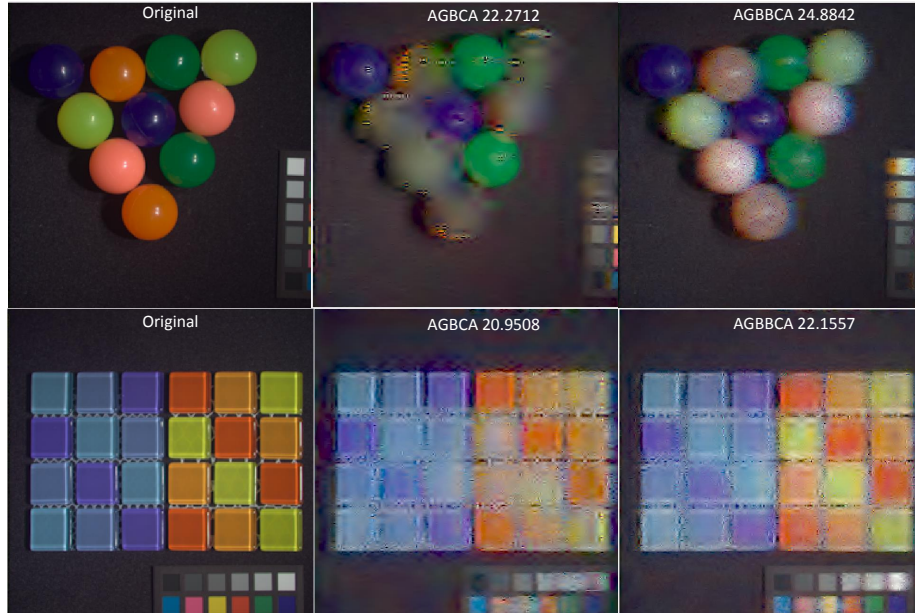

Figure 10: RGB reconstruction of Superballs and Glass-Tiles scenes using 8 snapshots, percentage of saturation of 10% and a compression ration of 50% for AGBCA the average PSNR 22.2712 dB, and 20.9508 dB for the Superballs and Glass-Tiles, respectively. With a compression ration of 26%, the average PSNR for AGBBCA is 24.8842 dB and 22.1557 dB for the Superballs and Glass-Tiles, respectively.

The Fig. 11 depicts the comparison of quality of image reconstruction using the AGBCA, and the proposed AGBBCA using two databases Superballs and Glass-Tiles. The number of snapshots is $\ell = \{1, 3, 5, 7\}$, the percentage of saturation using in this experiment is 20%, and the percentage of noise is $SNR = 10$ dB. The first and third rows show the reconstructed images using the AGBCA. The second and fourth rows show the reconstructed images using the AGBBCA. Notice that both methods attain low reconstructed quality with one snapshot because at this point the saturation is highest due to no attenuation. Notice that as the number of snapshots increases the quality of images reconstruction of the proposed methods improves.

5. Experimental setup

The proposed system uses a DMD-based implementation to emulate the grayscale coded apertures, the experimental setup is a variation of [27], [28]. The structure of the system has two arms, the imaging arm, and the integration arm. The imaging arm is composed of an objective lens that focuses the scene in the image plane of the DMD. Elements in the integration arm are rotated 45°, this comprises the relay lens, disperser, and the detector. The emulation of the system requires a synchronization control of grayscale coded aperture by setting correctly the duty cycle of the DMD to generate grayscale patterns. In more detail, the duty cycle in the DMD is defined in terms of percentage by $D = \dfrac{P}{I} \times 100\%$, where P is the width of the pulse that moves on the micromirrors, and I is the integration time of the detector, emulating $T^{\ell}_{m,n}$ in Eq. (3). The grayscale coded aperture is calibrated to attain the impulse response of the arrangement by using a white plate and a monochromatic light along the spectral range of interest. The compressive measurements are obtained using the real scene rather than the white plate, and a broadband white light instead of the monochromatic light.

The bottleneck in the experimentation occurs with the DMD switching time 50 μs, and the integration time of the detector 100 ms. An example of the
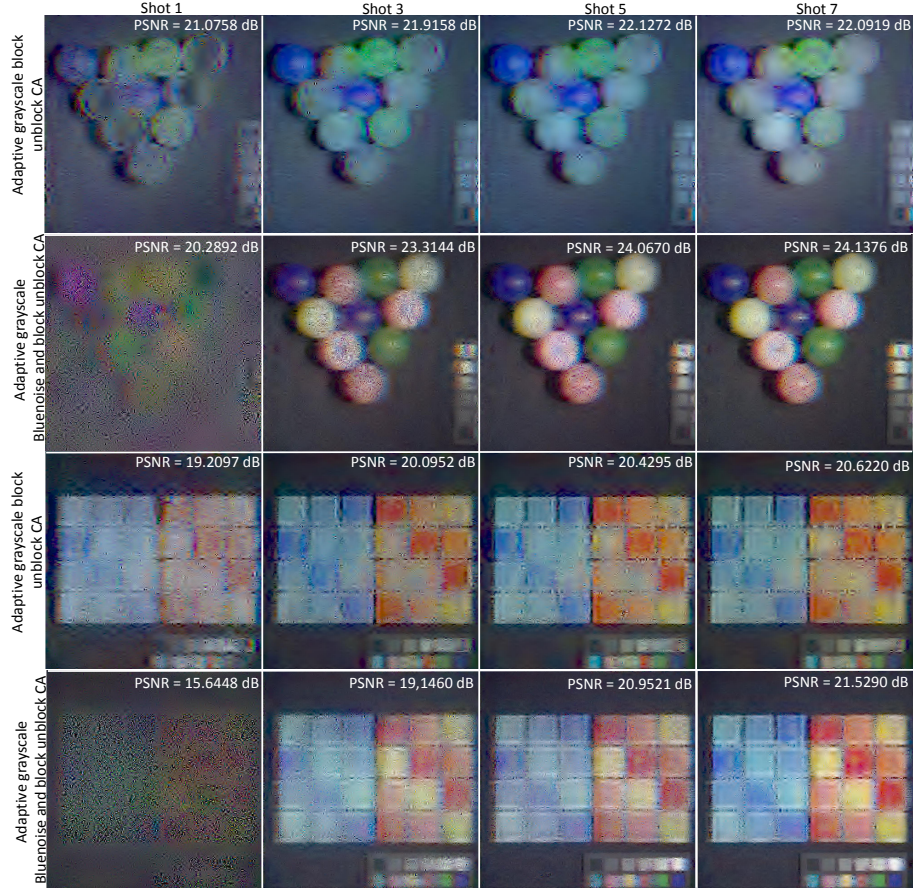
22

Figure 11: Comparison of reconstructed images between AGBBCA and AGBCA for $\ell = \{1, 3, 5, 7\}$ snapshots with Superballs, and Glass-Tiles database, and using 20% percentage of saturation in the compressive measurements. The first and third rows show reconstructed images using adaptive grayscale block-unblock CA. The second and fourth rows depict reconstructed images via adaptive grayscale blue noise and block-unblock CA. As the number of snapshots is closer to 7 snapshot the quality of image reconstruction of AGBBCA is higher than AGBCA.

synchronization control for two snapshots is depicted in Fig. 12, where the first snapshot $\mathbf{H}^0$ is captured during $100\ ms$ of the FPA integration time, the corresponding duty cycle is 50% and transmittance 0.5. In the second snapshot $\mathbf{H}^1$, the measurement is gathered during $100\ ms$ with a duty cycle of 25% and transmittances 0.25. In addition, the pattern rate for the block-unblock code aperture is higher $1 - bit - 22,727Hz$ than the framerate for grayscale code apertures pattern rates $8 - bit - 290Hz$ which bounds the grayscale levels of the DMD to 256.
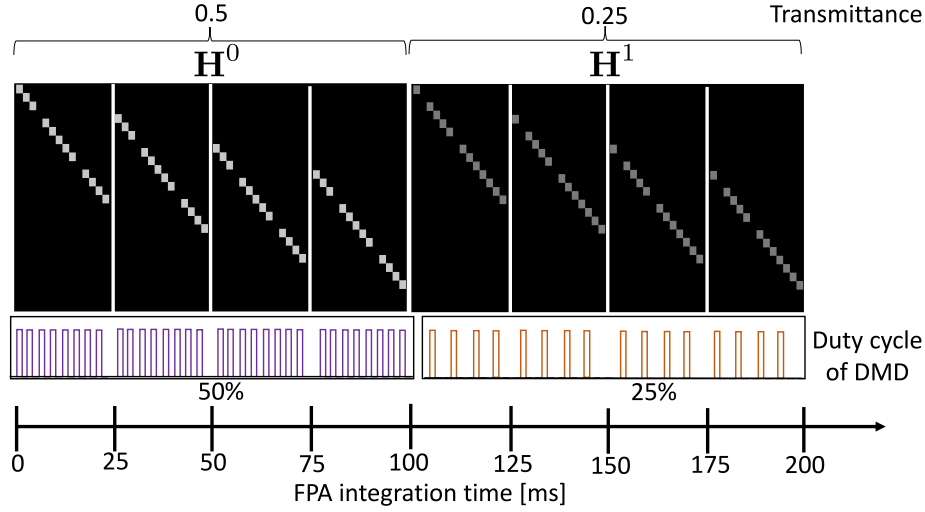

Figure 12: Two snapshot synchronization control. The first snapshot is captured during 100 ms corresponding to sensing matrix $\mathbf{H}^0$ which has a duty cycle of 50%. The second snapshot is captured in the following 100 ms corresponding to the sensing matrix $\mathbf{H}^1$ with duty cycle 25%. The transmittance values are 0.5, and 0.25, respectively.

In the system, the 2D grayscale coded aperture is loaded in the DMD. The dispersive element spreads the encoded light. Subsequently, the compressive measurements are attained in the array detector. The testbed implementation is synchronized such that the DMD settles the grayscale coding patterns and the detector captures the measurements. Afterwards, the DMD refreshes the coded aperture and the sensor captures the next measurements. The mechanism is composed by an AC254-100-A-ML objective lens (Thorlabs), a DLI4130 DMD (DLInnovations) with spatial resolution of 1024×768 and mirror pitch size of

13.68 μm, a MAP1100100-A relay lens (Thorlabs), an Amici Prism (Shanghai Optics) and a monochrome charged-coupled device detector (AVT Stingray F-145B) with spatial resolution 1388×1038 and pixel size of 6.45 μm.

The two target scenes Bear-stars and Flower-stars [28] are used to compare the proposed approach (AGBBCA) against the traditional (AGBCA). The target scenes have a spatial resolution of 128×128 and $L = 11$ spectral bands, corresponding to the wavelength intervals [423-436]; [437-448]; [449-463]; [464-479]; [480-499]; [500-521]; [522-546]; [547-577]; [578-618]; [619-673]; [674-700] nm. The spectral resolution depends on the pitch of the sensor and the dispersion function of the prism. The characterization of the double Amici dispersion prism function is similar to the used in [29]. The difference in the bandwidth is due to the non-linearity of the prism.

The first column of Fig. 13 shows the two targets. The Fig. 13 shows the spectral comparison for three spatial points in the Bear-stars and the Flowers-starts scenes. In more detail, the first row of Fig. 13 depicts the spectral signatures for the P1 [x=14, y=103] red bow tie, P2 [x=113, y=105] light-blue background, P3 [x=39, y=11] brown bear head. The presented results for Bears-stars scene correspond to 40% of saturation and using $K = 5$ snapshots. The second row in Fig. 13 shows the spectral signatures for the P1 [x=127, y=45] blue-light background, P2 [x=19, y=117] orange petal of the flower in the bottom-left corner, P3 [x=47, y=7] blue-light background. The presented results for Flowers-stars correspond to 30% of saturation and using $K = 7$ measurements. In each subplot, the black line corresponds to the ground-truth which is measured using an Ocean Optics Flame spectrometer. The captured spectral signature is compared against the reconstruction of the proposed adaptive method (AGBBCA) represented by the red line, for the bears-stars and the flower-starts scene, and the reconstruction of the traditional random method (AGBCA) denoted by the blue line.
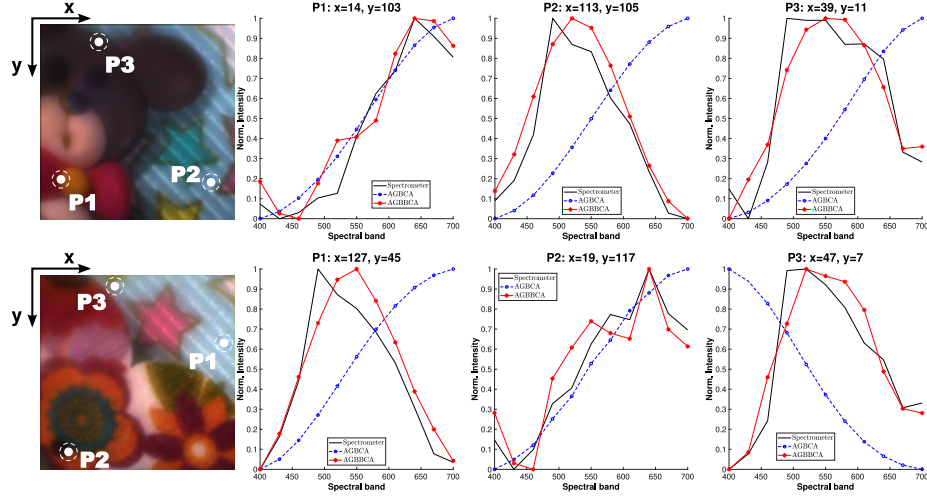
Figure 13: Reconstructions along the spectral axis for highlighted spatial locations in the two target scenes, using both AGBCA and AGBBCA coded apertures. The presented results for Bear-stars scene corresponds to 40% of saturation and using $K = 5$ measurement shots. The presented results for Flowers-stars scene corresponds to 30% of saturation and using $K = 7$ measurement shots.

6. Conclusions

The adaptive grayscale blue noise and block-unblock coded apertures (AG-BBCA) have been introduced in the CASSI system to replace the traditional adaptive grayscale block-unblock coded apertures (AGBCA). The proposed architecture allows attenuating the effect of the saturation of the FPA sensors while increasing the dynamic range of the system. The designed adaptive grayscale blue noise and block-unblock coded apertures outperform the adaptive grayscale block-unblock coded apertures in up to 2 dB in the quality of image reconstruction. Additionally, the proposed architecture has been implemented. The experimental results prove the spatial-spectral accuracy of the implemented design.

References

[1] G. Lu, B. Fei, Medical hyperspectral imaging: a review, Journal of Biomedical Optics 19 (1) (2014) 010901. doi:10.1117/1.JBO.19.1.010901.

₄₁₅   URL `http://dx.doi.org/10.1117/1.JBO.19.1.010901`

[2] A. F. Goetz, Three decades of hyperspectral remote sensing of the earth: A personal view, Remote Sensing of Environment 113, Supplement 1 (2009) S5 – S16, imaging Spectroscopy Special Issue. `doi:http://dx.doi.org/10.1016/j.rse.2007.12.014`.

₄₂₀   URL   `http://www.sciencedirect.com/science/article/pii/S003442570900073X`

[3] C. Hinojosa, H. Rueda, H. Arguello, Analysis of matrix completion algorithms for spectral image estimation from compressive coded projections, in: 2015 20th Symposium on Signal Processing, Images and Computer ₄₂₅ Vision (STSIVA), IEEE, 2015, pp. 1–7.

[4] C. A. Hinojosa, J. Bacca, H. Arguello, Spectral imaging subspace clustering with 3-d spatial regularizer, in: Digital Holography and Three-Dimensional Imaging, Optical Society of America, 2018, pp. JW5E–7.

[5] K. Sanchez, C. Hinojosa, H. Arguello, Supervised spatio-spectral classifica-₄₃₀ tion of fused images using superpixels, Applied optics 58 (7) (2019) B9–B18. `doi:10.1364/AO.58.0000B9`.
    URL `http://ao.osa.org/abstract.cfm?URI=ao-58-7-B9`

[6] G. R. Arce, D. J. Brady, L. Carin, H. Arguello, D. S. Kittle, Compressive coded aperture spectral imaging: An introduction, IEEE Signal Processing ₄₃₅ Magazine 31 (1) (2014) 105–115.

[7] A. Wagadarikar, R. John, R. Willett, D. Brady, Single disperser design for coded aperture snapshot spectral imaging, Applied optics 47 (10) (2008) B44–B51.

[8] D. Kittle, K. Choi, A. Wagadarikar, D. J. Brady, Multiframe image esti-₄₄₀ mation for coded aperture snapshot spectral imagers, Appl. Opt. 49 (36) (2010) 6824–6833. `doi:10.1364/AO.49.006824`.
    URL `http://ao.osa.org/abstract.cfm?URI=ao-49-36-6824`

[9] D. L. Donoho, Compressed sensing, IEEE Transactions on information theory 52 (4) (2006) 1289–1306.

[10] M. A. T. Figueiredo, R. D. Nowak, S. J. Wright, Gradient projection for sparse reconstruction: Application to compressed sensing and other inverse problems, Tech. rep., IEEE Journal of Selected Topics in Signal Processing (2007).

[11] C. V. Correa, C. Hinojosa, G. R. Arce, H. Arguello, Multiple snapshot colored compressive spectral imager, Optical Engineering 56 (4) (2016) 041309. `doi:10.1117/1.OE.56.4.041309`.
URL `https://doi.org/10.1117/1.OE.56.4.041309`

[12] Y. Wu, I. O. Mirza, G. R. Arce, D. W. Prather, Development of a digital-micromirror-device-based multishot snapshot spectral imaging system, Optics letters 36 (14) (2011) 2692–2694.

[13] H. Arguello, G. R. Arce, Rank minimization code aperture design for spectrally selective compressive imaging, IEEE Transactions on Image Processing 22 (3) (2013) 941–954. `doi:10.1109/TIP.2012.2222899`.

[14] H. F. Rueda Chacon, H. Arguello Fuentes, Spatial super-resolution in coded aperture- based optical compressive hyperspectral imaging systems, Revista Facultad de Ingenieria Universidad de Antioquia (2013) 7 – 18.
URL `http://www.scielo.org.co/scielo.php?script=sci_arttext&pid=S0120-62302013000200001&nrm=iso`

[15] H. Arguello, G. Arce, Colored coded aperture design by concentration of measure in compressive spectral imaging, IEEE Transactions on Image Processing 23 (4) (2014) 1896–1908. `doi:10.1109/TIP.2014.2310125`.

[16] C. Hinojosa, J. Bacca, H. Arguello, Coded aperture design for compressive spectral subspace clustering, IEEE Journal of Selected Topics in Signal Processing 12 (6) (2018) 1589–1600.

[17] J. N. Laska, P. T. Boufounos, M. A. Davenport, R. G. Baraniuk, Democracy in action: Quantization, saturation, and compressive sensing, Applied and Computational Harmonic Analysis 31 (3) (2011) 429 – 443. doi:http://dx.doi.org/10.1016/j.acha.2011.02.002.
URL http://www.sciencedirect.com/science/article/pii/S1063520311000248

[18] N. Diaz, H. R. Chacon, H. A. Fuentes, High-dynamic range compressive spectral imaging by grayscale coded aperture adaptive filtering, Ingeniería e Investigación 35 (3) (2015) 53–60.
URL http://www.revistas.unal.edu.co/index.php/ingeinv/article/view/49868

[19] N. Diaz, H. Rueda, H. Arguello, Adaptive uniform grayscale coded aperture design for high dynamic range compressive spectral imaging, in: Hyperspectral Imaging Sensors: Innovative Applications and Sensor Standards 2016, Vol. 9860, International Society for Optics and Photonics, 2016, p. 98600A.

[20] C. V. Correa, H. Arguello, G. R. Arce, Spatiotemporal blue noise coded aperture design for multi-shot compressive spectral imaging, JOSA A 33 (12) (2016) 2312–2322.

[21] Y. Kaganovsky, D. Li, A. Holmgren, H. Jeon, K. P. MacCabe, D. G. Politte, J. A. O'Sullivan, L. Carin, D. J. Brady, Compressed sampling strategies for tomography, JOSA A 31 (7) (2014) 1369–1394.

[22] D. L. Donoho, M. Elad, Optimally sparse representation in general (nonorthogonal) dictionaries via ℓ_1 minimization, Proceedings of the National Academy of Sciences 100 (5) (2003) 2197–2202.

[23] H. Arguello, G. R. Arce, Restricted isometry property in coded aperture compressive spectral imaging, in: Statistical Signal Processing Workshop (SSP), 2012 IEEE, IEEE, 2012, pp. 716–719.

[24] M. Ledoux, The concentration of measure phenomenon, no. 89, American Mathematical Soc., 2001.

[25] J. N. Laska, P. T. Boufounos, M. A. Davenport, R. G. Baraniuk, Democracy in action: Quantization, saturation, and compressive sensing, Applied and Computational Harmonic Analysis 31 (3) (2011) 429–443.

[26] D. L. Lau, G. R. Arce, Modern Digital Halftoning, Second Edition, CRC Press, Inc., Boca Raton, FL, USA, 2007.

[27] H. Rueda, H. Arguello, G. R. Arce, Dmd-based implementation of patterned optical filter arrays for compressive spectral imaging, J. Opt. Soc. Am. A 32 (1) (2015) 80–89. doi:10.1364/JOSAA.32.000080.
URL http://josaa.osa.org/abstract.cfm?URI=josaa-32-1-80

[28] N. Diaz, H. Rueda, H. Arguello, Adaptive filter design via a gradient thresholding algorithm for compressive spectral imaging, Appl. Opt. 57 (17) (2018) 4890–4900. doi:10.1364/AO.57.004890.
URL http://ao.osa.org/abstract.cfm?URI=ao-57-17-4890

[29] C. V. Correa, H. Arguello, G. R. Arce, Snapshot colored compressive spectral imager, J. Opt. Soc. Am. A 32 (10) (2015) 1754–1763. doi:10.1364/JOSAA.32.001754.
URL http://josaa.osa.org/abstract.cfm?URI=josaa-32-10-1754